Journal of the European Ceramic Society 38 (2018) 3325–3332

Contents lists available at ScienceDirect

Journal of the European Ceramic Society

journal homepage: www.elsevier.com/locate/jeurceramsoc

Original Article

Stage-sensitive microstructural evolution of nanostructured TBCs during thermal exposure

Guang-Rong Li[a,b], Guan-Jun Yang[a,*], Cheng-Xin Li[a], Chang-Jiu Li[a]

[a] State Key Laboratory for Mechanical Behavior of Materials, School of Materials Science and Engineering, Xi'an Jiaotong University, Xi'an, 710049, China
[b] State Key Laboratory for Manufacturing Systems Engineering, School of Mechanical Engineering, Xi'an Jiaotong University, 710049 Xi'an, China

ARTICLE INFO

Keywords:
Nanostructured TBCs
Two-stage trend
Sintering
Multiscale structural changes
Structural tailoring

ABSTRACT

Nanostructured thermal barrier coatings (TBCs) often exhibit bimodal structure comprised of both nanozones and lamellar zones, and therefore, their sintering behaviour can be different from that of conventional coatings. In this study, changes in the microstructure and properties of nanostructured TBCs were investigated. The results show that their microstructural evolution is highly time-sensitive during long thermal exposure at 1150 °C. In stage I (0–20 h), changes in mechanical properties were significant. The dominant microstructural change was faster healing of flat pores, whereas the macroscopic structure seemed less affected. In stage II (20–500 h), the changes in properties were much slighter and some large macroscopic voids appeared. In brief, the microscopic healing of pores in lamellar zones leads to a significant change in mechanical properties in stage I, whereas sintering of the nanozones leads to macroscopic voids in stage II.

1. Introduction

Thermal barrier coatings (TBCs) have been widely used in both aero and land-based gas turbines to protect their hot-section metallic components (e.g., combustion cans, blades and vanes) against high temperatures. TBCs often consist of a thermally resistant top coat and an oxidation-resistant bond coat applied on a metal substrate [1,2]. The top coat is typically prepared by plasma-sprayed yttria-stabilized zirconia ((PS-YSZ)), especially in land-based gas turbines [3,4]. Their lamellar structure with intersplat pores and intrasplat cracks contributes to excellent performance with respect to thermal insulation [5,6] and strain tolerance, the latter of which affects the lifetime of TBCs significantly [7,8].

There is an urgent demand for advanced TBCs to retard their degradation at high operating temperatures. Nanostructured materials are potentially attractive, as their mechanical performance can be considerably enhanced if their grain sizes are reduced from conventional microscale to nanoscale sizes (i.e., < 100 nm) [9,10]. The Hall–Petch empirical relationship (Eq. (1)) can be used to describe the improvement in mechanical properties by decreasing grain size [11]. For example, the hardness of pure nickel can be increased by a factor of six when decreasing the grain size from 1 μm to 10 nm [12]. Consequently, nanostructured powders have recently been widely used to prepare the top coat of TBCs [13–16].

$$A = A_0 + kd^{-1/2} \quad (1)$$

where A refers to the mechanical properties of the material (e.g., hardness, yield strength), the subscript 0 refers to the material's infinite grain size, k is a constant, which stands for the grain boundary as an obstacle to the propagation of deformation (metal) or a crack (ceramics), and d is the grain size.

For TBCs with a nanostructured top coat, it is crucial to retain the pre-existing nanostructure of the feedstock during the PS process [17], in order to achieve the desired performance level of the nanostructured materials. PS coatings are formed by successive deposition of fully and partially molten particles on a substrate followed by lateral flattening, rapid solidification and cooling [18,19]. The fully molten feedstock would result in typical lamellar zones similar to conventional coatings, whereas the partially molten feedstock may retain its nano-features [18,20]. Therefore, the presence of a partially molten feedstock is necessary for translating the excellent physical properties of the nanostructured feedstock to the coatings. As a result, the structure of PS nanostructured top coats can be described as semi-molten nanozones surrounded by fully molten lamellar zones. This morphology has been called a bimodal structure in previous reports [21,22]. In brief, in nanostructured YSZ coatings, typical lamellar zones and embedded nanozones coexist. Therefore, sintering behaviour of the coating would be intimately related to these two zones. Owing to their bimodal structure, nanostructured TBCs are reported to have superior reliability and

* Corresponding author.
E-mail address: ygj@mail.xjtu.edu.cn (G.-J. Yang).

https://doi.org/10.1016/j.jeurceramsoc.2018.03.019
Received 6 September 2017; Received in revised form 6 March 2018; Accepted 14 March 2018
Available online 15 March 2018

lifetime in comparison to conventional TBCs, both in isothermal cyclic tests [23–25] and gradient thermal cyclic tests [26]. The reason is qualitatively attributed to the formation of coarse voids, which counteracts the detrimental effect induced by sintering [27,28]. However, very little work has focused on the microstructural evolution of nanostructured TBCs with a bimodal structure during the sintering process, and thus a complete understanding of their sintering behaviour has not been developed.

The features of bimodal nanostructured YSZ coatings can be summarized as follows: (i) The matrix is the lamellar zone formed from the initially molten but subsequently solidified particles. The inner structure of the splat has a high density after resolidification from the molten state. However, similar to conventional (PS-YSZ) coatings [8,20], the stacking of splats leads to the formation of a lamellar structure with a network of flat (2D) pores. Intersplat pores correspond to imperfect bonding between layers, whereas intrasplat cracks are formed during the quenching process. Moreover, the lamellar zones are anisotropic structures owing to their unique grain orientation and pore shape [7,29]. (ii) The nanozones exhibit a loose and isotropic microstructure. The sintering mechanism of nanozones would be similar to that observed in conventional ceramic sintering or that described in powder metallurgy [30]. However, sintering of the matrix is much more structure- and material-specific. In short, anisotropic lamellar zones and isotropic nanozones may follow different sintering mechanisms. In addition, competition of sintering effects between the lamellar zones and the nanozones may modify the observed performance during the overall thermal exposure. Therefore, a comprehensive understanding of the sintering mechanism of the nanostructured TBCs would be very useful.

The objective of this study is to elucidate a comprehensive sintering mechanism for nanostructured TBCs. Multiscale changes in structure and properties during thermal exposure were investigated to understand the sintering behaviours of the lamellar zones and the nanozones. This fundamental study will help in the development of an optimized structure for advanced nanostructured TBCs.

2. Experimental procedure

2.1. Sample preparation and thermal exposure

Powder particles used for plasma spraying often exhibit a size distribution varying from 5 to 100 μm, which means that the feedstock powders are microsized. Nanoparticles, with a size distribution lower than 100 nm, cannot be subjected to plasma spraying directly using regular powder feeders. These tiny nanopowders would clog the insides of hoses and fittings used to transport powder particles from the powder feeder to the thermal spray torch. Therefore, it is necessary to agglomerate the nanosized particles before using regular powder feeders [16].

A commercially available nanostructured 7 wt% YSZ (Nanox S4007, Inframat corporation, Farmington, CT, USA) was used as the feedstock in this study. The size distribution of agglomerates is in the range of 50–150 μm (d_{10} = 53.7, d_{50} = 79.9, d_{90} = 152.4), whereas the nanosized YSZ particles making up the agglomerates have diameters varying from 50 to 150 nm. Nanostructured YSZ coatings were plasma sprayed on a stainless-steel substrate using a commercial plasma spray system (GP-80, 80 kW class, Jiujiang, China). Subsequently, free-standing YSZ samples were obtained by dissolving the substrate in a hydrochloric acid solution. The melting point of 7–8 wt% YSZ is reported to be approximately 2700 °C [27]. Plasma-spraying parameters were chosen based on a previous report [26], in order to obtain a bimodal microstructure with both lamellar zones and nanozones, as given in Table 1.

To examine the evolution of the microstructure and properties of YSZ coatings during thermal exposure, samples were heated in a furnace to 1150 °C, based on the fact that the general service temperature of TBCs is above 1000 °C. After holding at this temperature for various durations, the samples were cooled to room temperature. In order to avoid unexpected coating structure degradation by fast temperature change, the heating and cooling rates were fixed at a relatively low rate of 10 °C/min. Based on previous reports [31,32], significant formation of monoclinic phase often occurs at temperatures above 1200 °C. Therefore, it is reasonable to conclude that sintering at 1150 °C is relatively unaffected by phase change.

Table 1
Parameters used for plasma spraying.

Parameters	Value
Plasma arc voltage/V	60
Plasma arc current/A	650
Flow rate of primary gas (Ar)/L min^{-1}	80
Flow rate of secondary gas (H_2)/L min^{-1}	16
Flow rate of powder feeding gas (N_2)/L min^{-1}	4.5
Spray distance/mm	110
Torch traverse speed/mm s^{-1}	500

2.2. Microstructural characterization and mechanical property measurement

Surface and cross-sectional morphology of the coatings was examined using a scanning electron microscopy (SEM) system (TESCAN MIRA 3, Brno, Czech Republic). The apparent porosity contributed by microsized pores of the coatings was determined by image analysis using SEM backscattered electron imaging (BEI) on the polished cross sections. The aim of measuring porosity was to reveal the structural evolution of the bimodal nanostructured coatings. At least 20 images were used to estimate the porosity of each sample. In addition to the apparent porosity, 2D pore length densities were also determined after various durations of thermal exposure. The 2D pore length density (including intersplat pores and intrasplat cracks) is defined as the total length of 2D pores in a unit area. The total length of 2D pores was measured under a magnification of 5000×. For some difficult-to-measure pores, a higher magnification was used. The densities of intersplat pores and intrasplat cracks were obtained, respectively, from the polished cross section and surface of the coatings. For each sample, at least 50 SEM images were used. More details on the measurement of 2D pore density can be found elsewhere [33].

The microscopic elastic modulus of the YSZ coatings was determined using a Knoop indentation test system (Buehler Micromet 5104, Akashi Corporation, Japan). The test was performed at a test load of 300 gf and a holding time of 30 s [34]. For each condition (e.g., 10 h at 1150 °C), 3 similar samples were analysed and 20 randomly distributed spots were analysed for each sample.

The macroscopic elastic modulus in the in-plane direction was determined using a three-point bending (3PB) test system (Instron 5943, America). During the test, the elastic modulus was obtained from the following formulas:

$$w = \frac{PL^3}{48D} \tag{2}$$

$$D = \frac{Eh^3}{12(1-\nu^2)} \tag{3}$$

where P is the load applied at the middle of the span, L is the span between two supports, D is the bending stiffness, w is the central deflection, E is the elastic modulus of the coating, h is the coating thickness, and ν is the Poisson's ratio of the coating.

3. Results

3.1. Microstructure of the as-deposited coatings

SEM images of as-sprayed nanostructured YSZ coatings are shown in

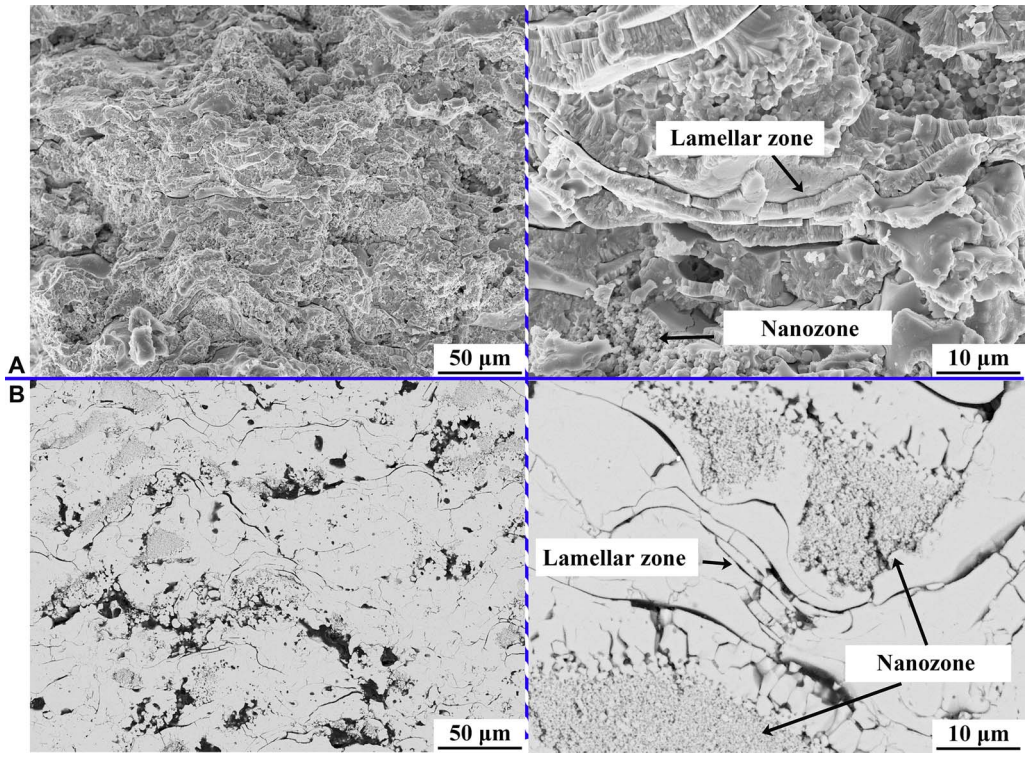

Fig. 1. Morphology of the as-deposited coatings: (A) fractured cross section and (B) polished cross section.

Fig. 1. In the case of the fractured cross section (see Fig. 1A), it can be seen that porous nanozones are surrounded by lamellar zones, exhibiting a typical bimodal structure similar to that reported in previous studies [16,22]. It is possible to recognize similarities between the nanozone and morphology of the feedstock, whereas the lamellar zones exhibit similar morphology to coatings produced from conventional microsized YSZ feedstock [8,35]. Columnar grains oriented along the deposition direction can clearly be seen in the splats. In the case of the polished cross sections (see Fig. 1B), the percentage area of nanozones is estimated to be approximately 20 to 25%, whereas the apparent porosity is ~10%.

3.2. Changes in mechanical property during thermal exposure

Changes in mechanical properties during thermal exposure are shown in Fig. 2. First, it can be observed that the macroscopic elastic modulus is distinctly lower than the microscopic elastic modulus. The reason for this is that the macroscopic elastic modulus is a global reflection of the strain tolerance of the whole coating structure. Second, the changes in macroscopic and microscopic elastic moduli show a similar trend. This trend shows that the rate of increase is initially much higher but slows down dramatically during the following extended thermal exposure stage. This means that the sintering kinetics of the nanostructured YSZ coatings is highly stage-sensitive. Third, the increment in elastic modulus at the initial shorter stage is significantly larger than that at the subsequent longer stage, as shown in Fig. 2(B, D). Finally, it is worth noting that the changes in microscopic elastic modulus were less significant than those of the macroscopic elastic modulus.

3.3. Effect of thermal exposure on microstructure

Fig. 3 shows images of polished cross-sections of YSZ coatings after progressively increasing the duration of thermal exposure. In the as-deposited state, it can be observed that the medium grey nanozones are surrounded by lighter lamellar zones. However, this contrast was more distinct after thermal exposure. This can be attributed to sintering occurring both in the lamellar zones and in the nanozones.

4. Discussion

4.1. Two-stage evolution trend of mechanical property

The elastic modulus of the plasma sprayed YSZ coatings are often less than 50% with respect to that of the bulk YSZ [4,35,36]. During thermal exposure, the mechanical property increased dramatically at the initial duration, after which the increase rate slowed down significantly (see Fig. 2). This suggests that the sintering behavior of nanostructured YSZ coatings is highly sensitive to the structural changes at different durations.

Fig. 4 shows the changes in elastic modulus as double logarithmic plots. To show the overall evolution, 0.1 h was used as the standing time for the as-sprayed state (corresponding to 0 h). It can be seen that the nonlinear trends are transformed into nearly linear trends. Moreover, the total evolution can be divided into approximately two stages, referred to as stage I and stage II. The boundary between the two stages is at approximately 20 h. The sintering kinetics are much higher in stage I than in stage II. It appears that most of the increase in elastic modulus has already occurred in stage I (~70%), as shown in Fig. 4(C, D). As the elastic modulus of PS-YSZ coatings depends on their unique structure [8], the stage-sensitive change may reflect the microstructural evolution of both lamellar zones and nanozones.

First, microstructural evolution at the lamellar zones was investigated. Fig. 5 shows the healing of pores and cracks from the fractured cross section and surface of lamellar zones. Pore healing over time can clearly be observed, despite the intersplat pores and intrasplat cracks. Consequently, the initial lamellar structure disappeared gradually and the splat was stiffened owing to the healing of intrasplat cracks; this phenomenon is consistent with previous reports [4,35]. Therefore, the healing of flat pores could be the primary reason for changes in elastic modulus during the overall process (see Fig. 2). Fig. 6 shows the statistical pore length density as a function of the thermal exposure

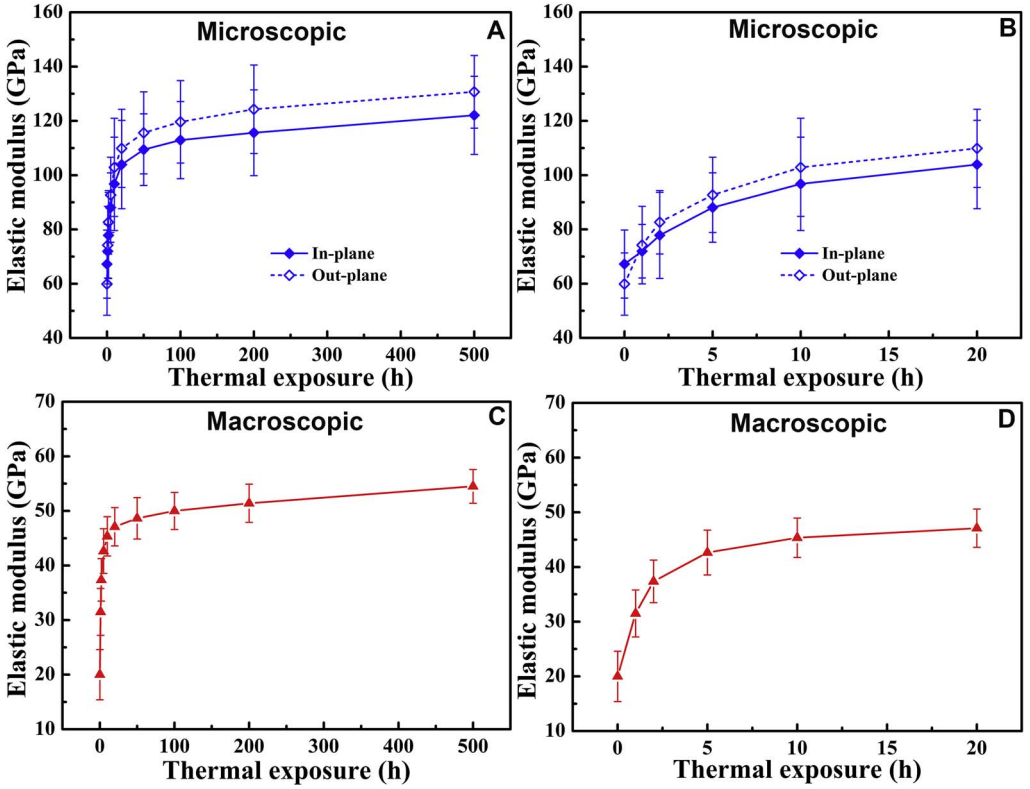

Fig. 2. Changes in mechanical property during thermal exposure: (A, B) microscopic elastic modulus, and (C, D) macroscopic elastic modulus.

duration. The densities of both intersplat pores and intrasplat cracks decreased significantly during thermal exposure.

4.2. Stage I: high sintering kinetic induced by pore healing

Considering the data from Fig. 6, the healing rate of intersplat pores is faster than that of intrasplat cracks in stage I. This is consistent with our previous reports on sintering of TBCs prepared by conventional microsized feedstocks [37,38]. The reasons for this are as follows: (i) Intersplat pores result from imperfect bonding between lamellar splats, whereas intrasplat cracks are generated from splat quenching [18,39]. Therefore, wide gaps and narrow gaps (pore tips) often co-exist in

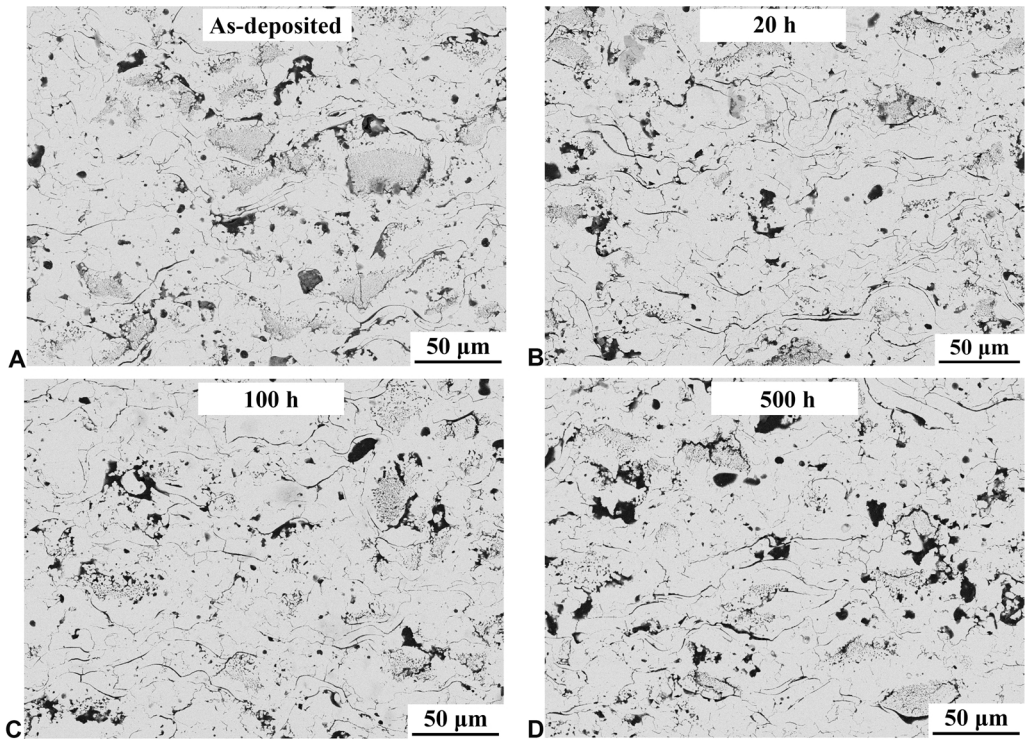

Fig. 3. Evolution of the polished cross-section of nanostructured YSZ coatings during thermal exposure.

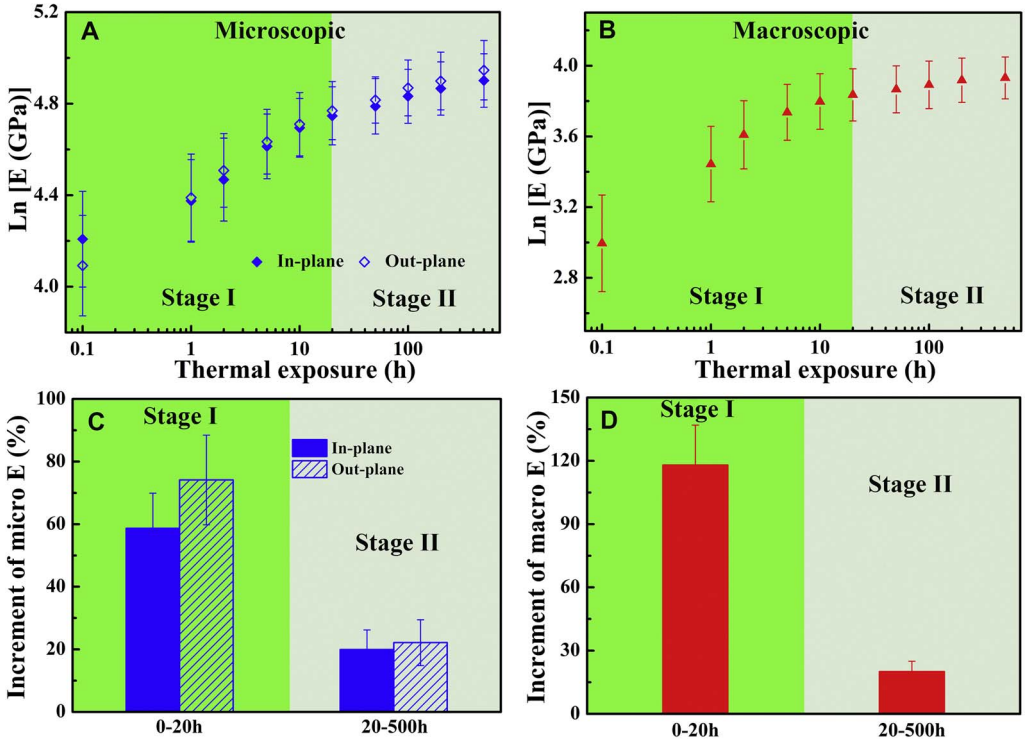

Fig. 4. Two-stage evolutionary trend in mechanical properties: (A) microscopic elastic modulus; (B) macroscopic elastic modulus; (C) increment of microscopic elastic modulus in the two stages; and (D) increment of macroscopic elastic modulus in the two stages.

intersplat pores. However, intrasplat cracks often separate splat segments completely in one layer. Very narrow intrasplat cracks (less than 100 nm) represent less than 10% of all intrasplat cracks [37], while nearly every intersplat pore has pore tips (narrow gaps). Therefore, the quantity of narrow gaps from intersplat pores is significantly higher than that from intrasplat cracks. (ii) During thermal exposure, formation of multipoint contacts between counter surfaces contributes to high sintering kinetics during stage I [37]. The narrow gaps provide a higher possibility for the counter-surface to be healed at multiple points. As a result, the sintering is driven by small radii of curvature. This would help explain why the healing of intersplat pores is faster than that of intrasplat cracks in stage I.

Fig. 7 shows in-situ healing behaviour of an intersplat pore. It can be seen that the smooth intersplat pore surface becomes rougher over time, consistent with a previous report [37]. The relatively smooth surface becomes roughened because of various mechanisms such as faceting of the grain surface, grooving of the bared grain boundary and columnar grains becoming convex [37]. These different mechanisms lead to different levels of roughness. The roughened surface creates new contacts with a counter surface, and then healing occurs at the pore tips. The sintering process is driven by a decrease in the free energy of the whole system. The number of contact points increases simultaneously during sintering, which accelerates matter transfer by multi-directional diffusion. This is different from conventional ceramic

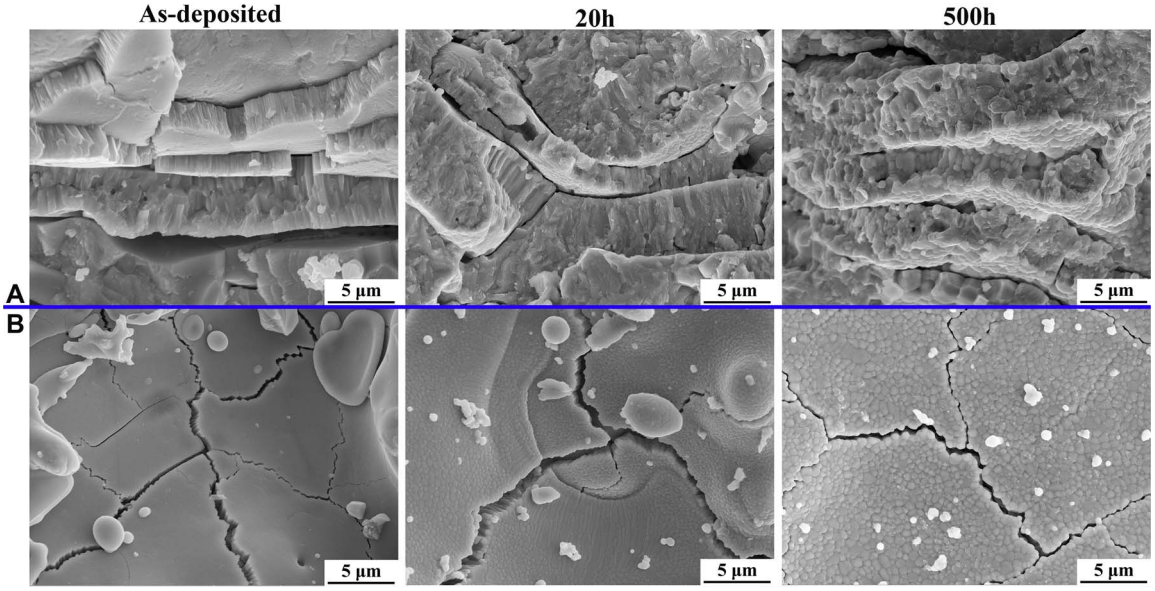

Fig. 5. Healing of the pores and cracks during thermal exposure: (A) intersplat pores and (B) intrasplat cracks.

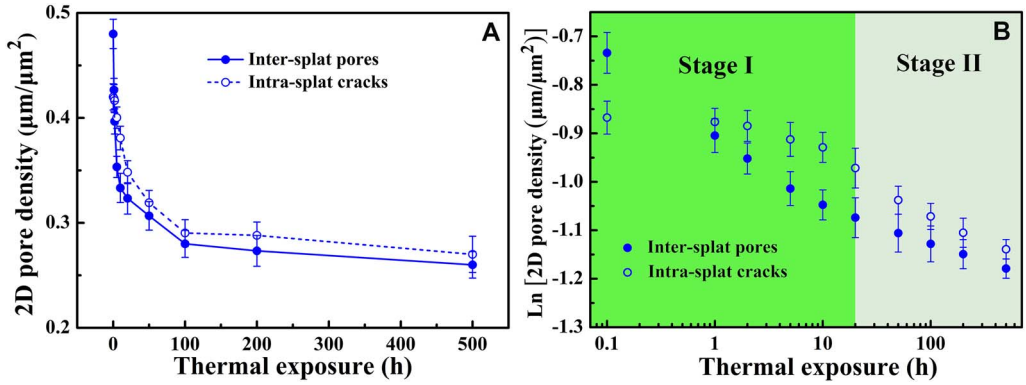

Fig. 6. Evolution of the pore length density as a function of thermal exposure durations: (A) 0–500 h and (B) double logarithmic curves.

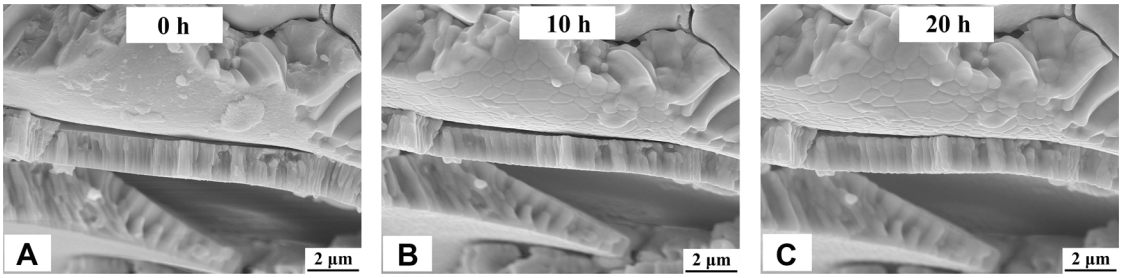

Fig. 7. In-situ healing observation of an intersplat pore during stage I: (A) 0 h, (B) 10 h, and (C) 20 h.

sintering or powder metallurgy mechanisms with single contact point [30]. Consequently, a much higher sintering rate occurs in stage I.

4.3. Stage II: densification of nanozones

The slower change rate of the elastic modulus in stage II can be discussed from two aspects. On the one hand, in the lamellar zones, the healing rate of intersplat pores slows significantly (see Fig. 6). According to our previous reports on the sintering of conventional TBCs [37,38], the number of contact points between counter surfaces decreases in stage II. Consequently, the transfer of matter slows down, as described in a previous study [20]. As a result, slower sintering kinetics are observed when the duration of thermal exposure is extended. This is the reason why some pores can still be observed in the polished cross section and at the surface even after thermal exposure for 500 h (see Fig. 5).

On the other hand, the nanozones also have a distinct effect on the evolution of the structure and properties during long thermal exposure. The nanozones are formed by embedding porous nanostructured agglomerates in the lamellar zones. Consequently, in addition to the typical pores that exist in conventional PS ceramic coatings [40,41], nanostructured YSZ coatings introduce a large quantity of nanopores in the nanozones. There is no doubt that these nanopores have a positive effect on the thermal insulation performance [26–28]. Moreover, the presence of nanopores increases the surface energy drastically [15]. Consequently, regarding sintering-induced densification, porous nanozones exhibit a much higher driving force than that of the lamellar zones. Fig. 8 shows the interfacial evolution between lamellar zones and nanozones during thermal exposure. It can be seen that linking between nanozones and lamellar zones occurs at some points. Consequently, the nanozones decrease as a function of thermal exposure duration (see Fig. 3). This is consistent with a previous report [42]. Moreover, the different densification rates and directions can contribute to the formation of an opening at the interface between porous nanozones and lamellar zones, resulting in some coarse voids in an apparent view, as shown in Fig. 9. The change in apparent porosity after thermal exposure is shown in Fig. 10. It shows that the apparent porosity decreases during the initial stage (0–20 h). After a longer thermal exposure (> 100 h), the apparent porosity exhibits a slight increase. This is distinctly different from that observed in conventional YSZ coatings [35]. In the as-deposited state, the observed large pores mainly arise from the spalling-off of weakly bonded splats during sample preparation [43,44]. After thermal exposure during stage I, lamellar bonding is enhanced significantly, because of which the apparent porosity decreases. During stage II, thermal exposure leads to differential sintering rates for the nanozones and the lamellar zones. The appearance of some coarse voids further increases the apparent porosity. In brief, the apparent porosity decreased distinctly in stage I owing to healing of intersplat pores, whereas it increased slightly in stage II.

To sum up, the sintering behaviour of nanostructured YSZ coatings actually reflects the combined behaviour of lamellar zones and nanozones. At lamellar zones, sintering leads to a significant healing of flat pores, particularly during stage I. Consequently, the elastic modulus increases dramatically. At nanozones, a much lower activation energy leads to a higher densification rate than in the lamellar zones. The appearance of coarse voids opposes the general trend of the disappearance of the nanopores between nanoparticles. Based on the above discussion, this comprehensive mechanism of sintering retards the loss of thermal insulation [16,27,28].

By understanding the comprehensive sintering mechanism of nanostructured TBCs, it is possible to achieve structural tailoring towards advanced TBCs. It may be an effective way to introduce some in-plane pores at a relatively large scale, and thus healing through multipoint connections would be weakened. Nanozones may be a potential way to create some large-scale pores during thermal exposure. Based on this consideration, highly sintering-resistant coating could be realized. It is worth noting that these large pores would inevitably compromise the fracture toughness of coatings. Therefore, more detailed work is necessary to balance the performance between thermal insulation and lifetime, to realize structural optimization.

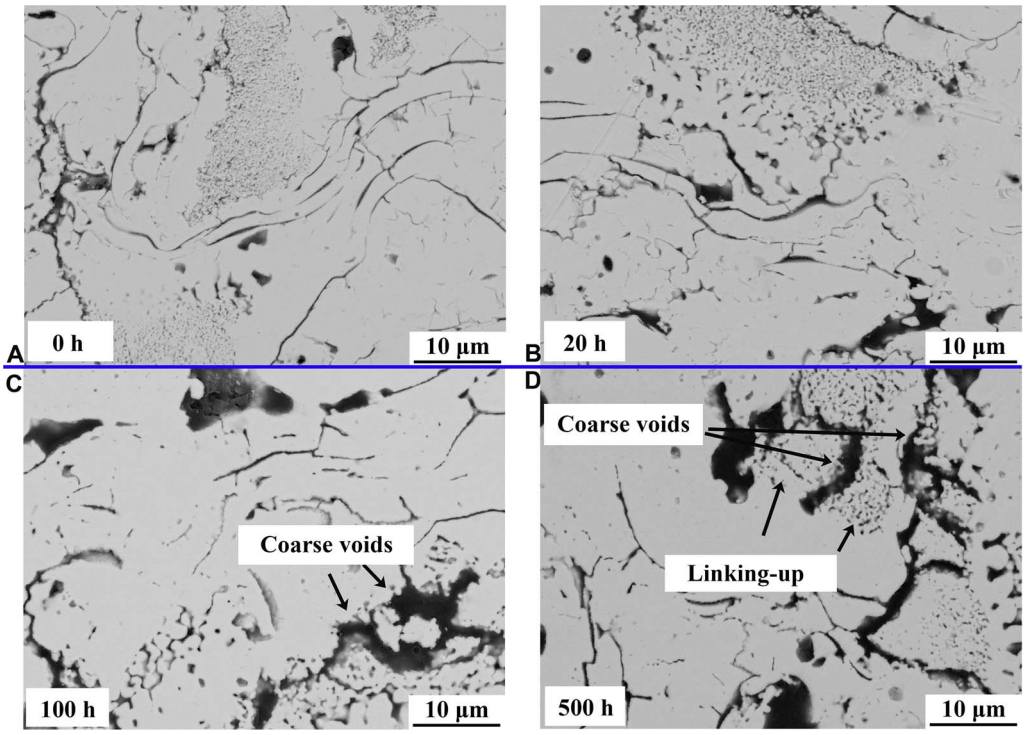

Fig. 8. Evolution of the interface between lamellar zones and nanozones during thermal exposure.

5. Conclusions

A detailed examination of the sintering behaviour of nanostructured YSZ coatings was carried out in this study. Lamellar zones and nanozones present different sintering mechanisms. Changes in structure and properties result from the combined effect of these two mechanisms. The detailed conclusions are as follows:

(i) Thermal exposure leads to a significant increase in micro- and macro-scopic elastic moduli. Furthermore, the observed increase exhibits a clear two-stage trend. The change rate during stage I is distinctly higher than that in the following stage II.

(ii) In stage I, the ultrafast sintering kinetics can be attributed primarily to the healing of intersplat pores through multipoint contact at the lamellar zones. This is the unique sintering characteristic of PS-YSZ coatings.

(iii) In stage II, the much slower sintering kinetics are attributed to two aspects. On the one hand, pore healing slows at the lamellar zones. On the other hand, differential sintering rates of lamellar zones and nanozones contribute to the formation of an opening at the interface of these two zones. Consequently, some coarse voids appear, retarding the loss of thermal insulation.

(iv) An understanding of the comprehensive sintering mechanism of nanostructured YSZ coatings could provide some directions for structural tailoring of TBCs, with the aim of achieving high thermal insulation performance.

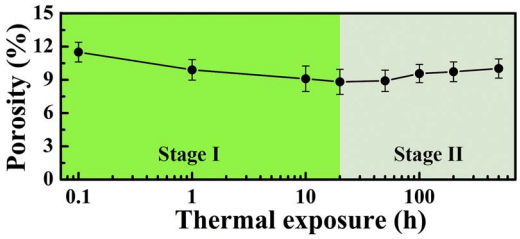

Fig. 10. Changes in apparent porosity as a function of thermal exposure duration.

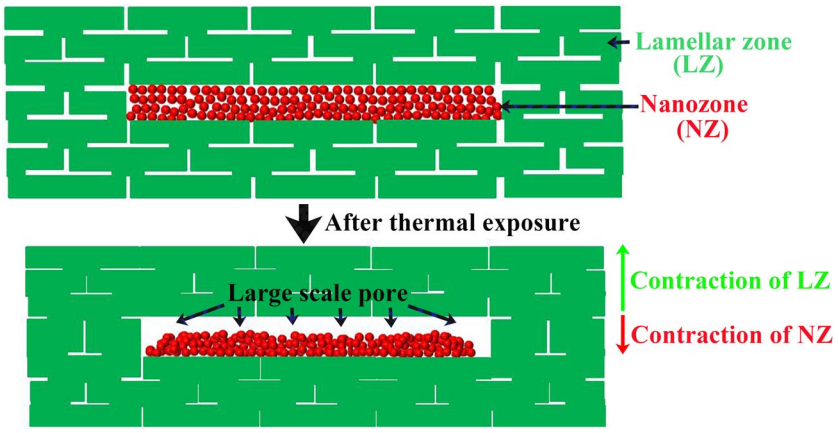

Fig. 9. Formation of a large-scale pore between a lamellar zone and a nanozone.

Acknowledgments

The present project was supported by the National Science Foundation of China (Grant No. 51671159), the National Basic Research Program of China (No. 2013CB035701), the Fundamental Research Funds for the Central Universities, and the National Program for Support of Top-notch Young Professionals.

References

[1] J.T. Demasimarcin, D.K. Gupta, Protective coatings in the gas-turbine engine, Surf. Coat. Tech. 68 (1994) 1–9.
[2] J. Ilavsky, G.G. Long, A.J. Allen, C.C. Berndt, Evolution of the void structure in plasma-sprayed YSZ deposits during heating, Mat. Sci. Eng. A-Struct. 272 (1) (1999) 215–221.
[3] J.M. Drexler, K. Shinoda, A.L. Ortiz, D.S. Li, A.L. Vasiliev, A.D. Gledhill, S. Sampath, N.P. Padture, Air-plasma-sprayed thermal barrier coatings that are resistant to high-temperature attack by glassy deposits, Acta Mater. 58 (20) (2010) 6835–6844.
[4] J.A. Thompson, T.W. Clyne, The effect of heat treatment on the stiffness of zirconia top coats in plasma-sprayed TBCs, Acta Mater. 49 (9) (2001) 1565–1575.
[5] H. Xie, Y.C. Xie, G.J. Yang, C.X. Li, C.J. Li, Modeling thermal conductivity of thermally sprayed coatings with intrasplat cracks, J. Therm. Spray Technol. 22 (8) (2013) 1328–1336.
[6] I.O. Golosnoy, A. Cipitria, T.W. Clyne, Heat transfer through plasma-sprayed thermal barrier coatings in gas turbines: a review of recent work, J. Therm. Spray Technol. 18 (5–6) (2009) 809–821.
[7] Y. Tan, A. Shyam, W.B. Choi, E. Lara-Curzio, S. Sampath, Anisotropic elastic properties of thermal spray coatings determined via resonant ultrasound spectroscopy, Acta Mater. 58 (16) (2010) 5305–5315.
[8] G.R. Li, B.W. Lv, G.J. Yang, W.X. Zhang, C.X. Li, C.J. Li, Relationship between lamellar structure and elastic modulus of thermally sprayed thermal barrier coatings with intra-splat cracks, J. Therm. Spray Technol. 24 (8) (2015) 1355–1367.
[9] M. Gell, Application opportunities for nanostructured materials and coatings, Mat. Sci. Eng. A-Struct. 204 (1–2) (1995) 246–251.
[10] R.W. Siegel, Nanostructured materials - mind over matter, Nanostruct. Mater. 3 (1–6) (1993) 1–18.
[11] Y.L. Lu, P.K. Liaw, The mechanical properties of nanostructured materials, Jom-J. Min. Met. Mat. Soc. 53 (3) (2001) 31–35.
[12] J. Hu, Y.N. Shi, X. Sauvage, G. Sha, K. Lu, Grain boundary stability governs hardening and softening in extremely fine nanograined metals, Science 355 (6331) (2017) 1292–1296.
[13] H. Chen, C.X. Ding, Nanostructured zirconia coating prepared by atmospheric plasma spraying, Surf. Coat. Technol. 150 (1) (2002) 31–36.
[14] Y. Zeng, S.W. Lee, L. Gao, C.X. Ding, Atmospheric plasma sprayed coatings of nanostructured zirconia, J. Eur. Ceram. Soc. 22 (3) (2002) 347–351.
[15] N. Wang, C.N. Zhou, S.K. Gong, H.B. Xu, Heat treatment of nanostructured thermal barrier coating, Ceram. Int. 33 (6) (2007) 1075–1081.
[16] R.S. Lima, B.R. Marple, Thermal spray coatings engineered from nanostructured ceramic agglomerated powders for structural, thermal barrier and biomedical applications: a review, J. Therm. Spray Technol. 16 (1) (2007) 40–63.
[17] R.S. Lima, A. Kucuk, C.C. Berndt, Integrity of nanostructured partially stabilized zirconia after plasma spray processing, Mat. Sci. Eng. A-Struct. 313 (1-2) (2001) 75–82.
[18] C.J. Li, A. Ohmori, Relationships between the microstructure and properties of thermally sprayed deposits, J. Therm. Spray Technol. 11 (3) (2002) 365–374.
[19] G.J. Yang, C.X. Li, S. Hao, Y.Z. Xing, E.J. Yang, C.J. Li, Critical bonding temperature for the splat bonding formation during plasma spraying of ceramic materials, Surf. Coat. Technol. 235 (2013) 841–847.
[20] A. Cipitria, I.O. Golosnoy, T.W. Clyne, A sintering model for plasma-sprayed zirconia TBCs. Part I: free-standing coatings, Acta Mater. 57 (4) (2009) 980–992.
[21] M. Gell, E.H. Jordan, Y.H. Sohn, D. Goberman, L. Shaw, T.D. Xiao, Development and implementation of plasma sprayed nanostructured ceramic coatings, Surf. Coat. Tech. 146 (2001) 48–54.
[22] R.S. Lima, A. Kucuk, C.C. Berndt, Bimodal distribution of mechanical properties on plasma sprayed nanostructured partially stabilized zirconia, Mat. Sci. Eng. A-Struct. 327 (2) (2002) 224–232.
[23] B. Liang, C.X. Ding, Thermal shock resistances of nanostructured and conventional zirconia coatings deposited by atmospheric plasma spraying, Surf. Coat. Technol. 197 (2-3) (2005) 185–192.
[24] C.B. Liu, Z.M. Zhang, X.L. Jiang, M. Liu, Z.H. Zhu, Comparison of thermal shock behaviors between plasma-sprayed nanostructured and conventional zirconia thermal barrier coatings, Trans. Nonferr. Metal. Soc. 19 (1) (2009) 99–107.
[25] W.Q. Wang, C.K. Sha, D.Q. Sun, X.Y. Gu, Microstructural feature, thermal shock resistance and isothermal oxidation resistance of nanostructured zirconia coating, Mat. Sci. Eng. A-Struct. 424 (1–2) (2006) 1–5.
[26] J. Wu, H.B. Guo, L. Zhou, L. Wang, S.K. Gong, Microstructure and thermal properties of plasma sprayed thermal barrier coatings from nanostructured YSZ, J. Therm. Spray Techn. 19 (6) (2010) 1186–1194.
[27] R. Lima, B. Marple, Toward highly sintering-resistant nanostructured ZrO_2-7 wt.% Y_2O_3 coatings for TBC applications by employing differential sintering, J. Therm. Spray Techn. 17 (5–6) (2008) 846–852.
[28] R.S. Lima, B.R. Marple, Nanostructured YSZ thermal barrier coatings engineered to counteract sintering effects, Mat. Sci. Eng. A-Struct. 485 (1-2) (2008) 182–193.
[29] F. Cernuschi, P. Bison, S. Marinetti, E. Campagnoli, Thermal diffusivity measurement by thermographic technique for the non-destructive integrity assessment of TBCs coupons, Surf. Coat. Technol. 205 (2) (2010) 498–505.
[30] G.C. Kuczynski, Self-diffusion in sintering of metallic particles, Trans. Am. I. Min. Met. Eng. 185 (2) (1949) 169–178.
[31] G.J. Yang, Z.L. Chen, C.X. Li, C.J. Li, Microstructural and mechanical property evolutions of plasma-sprayed YSZ coating during high-temperature exposure: comparison study between 8YSZ and 20YSZ, J. Therm. Spray Technol. 22 (8) (2013) 1294–1302.
[32] J. Ilavsky, J.K. Stalick, Phase composition and its changes during annealing of plasma-sprayed YSZ, Surf. Coat. Tech. 127 (2–3) (2000) 120–129.
[33] T. Liu, X.T. Luo, X. Chen, G.J. Yang, C.X. Li, C.J. Li, Morphology and size evolution of interlamellar two-dimensional pores in plasma-sprayed $La_2Zr_2O_7$ coatings during thermal exposure at 1300 °C, J. Therm. Spray Techn. 24 (5) (2015) 739–748.
[34] R.S. Lima, S.E. Kruger, G. Lamouche, B.R. Marple, Elastic modulus measurements via laser-ultrasonic and Knoop indentation techniques in thermally sprayed coatings, J. Therm. Spray Technol. 14 (1) (2005) 52–60.
[35] S. Paul, A. Cipitria, S.A. Tsipas, T.W. Clyne, Sintering characteristics of plasma sprayed zirconia coatings containing different stabilisers, Surf. Coat. Technol. 203 (8) (2009) 1069–1074.
[36] S. Karthikeyan, V. Balasubramanian, R. Rajendran, Developing empirical relationships to estimate porosity and Young's modulus of plasma sprayed YSZ coatings, Appl. Surf. Sci. 296 (2014) 31–46.
[37] G.R. Li, H. Xie, G.J. Yang, G. Liu, C.X. Li, C.J. Li, A comprehensive sintering mechanism for TBCs-Part I: an overall evolution with two-stage kinetics, J. Am. Ceram. Soc. 100 (5) (2017) 2176–2189.
[38] G.R. Li, H. Xie, G.J. Yang, G. Liu, C.X. Li, C.J. Li, A comprehensive sintering mechanism for TBCs-Part II: multiscale multipoint interconnection-enhanced initial kinetics, J. Am. Ceram. Soc. 100 (9) (2017) 4240–4251.
[39] T.W. Clyne, S.C. Gill, Residual stresses in thermal spray coatings and their effect on interfacial adhesion: a review of recent work, J. Therm. Spray Technol. 5 (4) (1996) 401–418.
[40] R. McPherson, On the formation of thermally sprayed alumina coatings, J. Mater. Sci. 15 (12) (1980) 3141–3149.
[41] P. Bengtsson, T. Johannesson, Characterization of microstructural defects in plasma-sprayed thermal barrier coatings, J. Therm. Spray Technol. 4 (3) (1995) 245–251.
[42] Y. Wang, Y. Bai, K. Liu, J.W. Wang, Y.X. Kang, J.R. Li, H.Y. Chen, B.Q. Li, Microstructural evolution of plasma sprayed submicron-/nano-zirconia-based thermal barrier coatings, Appl. Surf. Sci. 363 (2016) 101–112.
[43] J.F. Li, C.X. Ding, Polishing-induced pull outs of plasma sprayed Cr_3C_2-NiCr coating, J. Mater. Sci. Lett. 18 (21) (1999) 1719–1721.
[44] G.J. Yang, C.J. Li, C.X. Li, K. Kondoh, A. Ohmori, Improvement of adhesion and cohesion in plasma-sprayed ceramic coatings by heterogeneous modification of nonbonded lamellar interface using high strength adhesive infiltration, J. Therm. Spray Technol. 22 (1) (2013) 36–47.